



1 **Rapid formation of hydroxymethyl hydroperoxide and its vital role in**
2 **methanesulfonic acid-methylamine nucleation: impacts of urban industrial and**
3 **forested areas**

4 Rongrong Li ‡, Zeyao Li ‡, Chengyan Zhang, Rui Wang*, Jihuan Yang, Heran Cui, Xuanye Li, Nini Huo,
5 Tianlei Zhang*

6 *Institute of Theoretical and Computational Chemistry, Shaanxi Key Laboratory of Catalysis, School of Chemical &*
7 *Environment Science, Shaanxi University of Technology, Hanzhong, Shaanxi, 723000, P. R. China*

8
9
10 **Abstract**

11 Organic peroxides are widely recognized as important contributors to secondary organic aerosols formation.
12 Among these, hydroxymethyl hydroperoxide (HMHP) is a common species found in both the gas phase and fine
13 aerosols. Despite its abundance, the molecular-level formation of HMHP through methanesulfonic acid (MSA)-
14 catalyzed hydrolysis of CH₂OO, particularly in the gas phase and at the air-water interface, remains insufficiently
15 examined. Moreover, the role of HMHP in new particle formation (NPF) has not been fully elucidated. Herein, we
16 employ quantum chemical calculations together with Born-Oppenheimer molecular dynamics simulations to
17 investigate HMHP formation from CH₂OO hydrolysis with MSA under both gas phase and interfacial conditions.
18 Our results show that HMHP forms rapidly and stably in both environments. Further analysis using the atmospheric
19 cluster dynamics code reveals that HMHP not only enhances the clustering stability of MSA-methylamine (MA)
20 clusters, but also exerts a direct role in promoting MSA-MA nucleation. Importantly, in regions with elevated HMHP
21 concentrations (3.00×10^{10} - 1.25×10^{11} molecules·cm⁻³), such as Niwot Ridge and Southeastern United States, the
22 HMHP-involved pathways contribute unexpectedly up to 42% and 59% of total nucleation flux at 258.15 K,
23 respectively. These findings provide new insights into HMHP formation pathways and the efficient MSA-MA-
24 HMHP nucleation mechanism, offering a plausible explanation for the frequent and intense NPF events observed
25 in continental regions.

26 **Keywords:** hydroxymethyl hydroperoxide; gas phase; interfacial; new particle formation

27

* Corresponding authors. Tel: +86-0916-2641083, Fax: +86-0916-2641083.

e-mail: wangrui830413@163.com (R. Wang) ztianlei88@163.com (T. L. Zhang)

‡ These authors contributed equally to this work.



28 1. Introduction

29 Organic peroxides serve as important reactive intermediates in atmospheric oxidation processes, facilitating
30 free radical chain termination, oxidant cycling, and the formation of aerosols (Wang et al., 2023; Tröstl et al., 2016).
31 Among these, hydroxymethyl hydroperoxide (HMHP), a product of the hydrolysis of the simplest and highest
32 concentrations of reactive intermediates (CH_2OO), has been detected at notable concentrations in the atmosphere (Lee
33 et al., 1993; Nguyen et al., 2015). Atmospheric concentrations of HMHP typically range around 10^9 molecules· cm^{-3}
34 in locations such as Central Portugal (Jackson and Hewitt, 1996), Pabstthum (Grossmann et al., 2003) and Beijing
35 (Yi, 2000). However, in regions like Guangzhou (Zhang et al., 2001) and Niwot Ridge (Hewitt and Kok, 1991),
36 these levels can increase to approximately 10^{10} molecules· cm^{-3} . Notably, in the forests of the Southeastern United
37 States (Allen et al., 2018), concentrations can even reach up to 10^{11} molecules· cm^{-3} . Due to its high abundance,
38 HMHP undergoes subsequent reactions with other atmospheric species, leading to the formation of hydroperoxides,
39 organic peroxides, and secondary organic aerosols, which play a crucial role in influencing air quality, climate
40 forcing, and human health (Sakamoto et al., 2013; Rissanen et al., 2014). So, understanding the source of HMHP
41 and its impact on the atmospheric environment has become a major topic of significant interest in atmospheric
42 chemistry.

43 The hydrolysis of CH_2OO has been widely investigated using both experimental (Chao et al., 2015; Stone et
44 al., 2014; Berndt et al., 2015) and theoretical (Wu et al., 2023a; Lin et al., 2016; Wu et al., 2023b) approaches across
45 various temperature ranges. Experimental data (Chao et al., 2015; Ouyang et al., 2013) estimate the rate constant
46 for the direct CH_2OO hydrolysis to form HMHP to be approximately 4×10^{-15} cm^3 molecule $^{-1}$ s $^{-1}$. In contrast,
47 hydrolysis involving the water dimer ($(\text{H}_2\text{O})_2$) has rate constants between 4×10^{-12} and 8.9×10^{-12} cm^3 molecule $^{-1}$
48 s $^{-1}$ at 294-298 K (Lin et al., 2016; Berndt et al., 2015), approximately three orders of magnitude higher than that of
49 the reaction with monomeric water, demonstrating that the presence of the water dimer significantly enhances the
50 hydrolysis rate (Long et al., 2016; Anglada and Solé, 2016; Newland et al., 2015). Additionally, quantum chemical
51 calculations have shown that atmospheric organic amines, acids, and alcohols can catalyze CH_2OO hydrolysis by
52 substantially lowering activation barriers and accelerating reaction rates (Zhang et al., 2018; Chao et al., 2019).
53 However, the role of methanesulfonic acid (MSA) in facilitating CH_2OO hydrolysis remains underexplored, even
54 through the calculations reported by several groups (Li et al., 2024c; Wang et al., 2025) have shown that MSA is a
55 notably effective catalyst in both CH_3CHOO and HNSO_2 hydrolysis. In fact, atmospheric concentrations of MSA
56 are relatively elevated in both coastal and continental regions, varying from 10% to 250% of sulfuric acid levels (Yan



57 et al., 2019; Ning et al., 2022; Wei et al., 2024). So, the lack of understanding of the MSA-catalyzed CH₂OO
58 hydrolysis reaction mechanism limits the accurate understanding and evaluation of HMHP formation, especially in
59 regions with high MSA pollution concentrations.

60 Interfacial reactions at the air-water interface complement gas-phase reactions and can significantly influence
61 reaction rates (Xu et al., 2024; Fang et al., 2024). These interfacial reactions may involve distinct mechanisms, with
62 interfacial water molecules not only serving as reactive sites but also participating directly as reactants, proton
63 transfer mediators, and both donors and acceptors (Tang et al., 2024). For example, MSA-assisted HNSO₂
64 hydrolysis at the air-water interface follows two distinct reaction mechanisms, the ion-forming mechanism and the
65 proton exchange mechanism, resulting in the formation of the SFA···H₃O⁺ ion pair. This contrasts with the gas-
66 phase production of SFA formed from the MSA-catalyzed hydrolysis of HNSO₂ (Wang et al., 2025). In addition,
67 the reaction between glyoxal and dimethylamine proceeds 5.70×10^4 times more rapidly at aqueous interfaces
68 compared to the gas phase, where it is less likely to take place (Dong et al., 2024). Therefore, based on gas-phase
69 reactions, it is essential to investigate the MSA-catalyzed CH₂OO hydrolysis reaction mechanisms at the air-water
70 interface, which will enrich the understanding of HMHP sources in regions affected by MSA pollution.

71 MSA, structurally and chemically similar to the atmospheric aerosol nucleating precursor H₂SO₄, is regarded
72 as an important nucleating precursor for new particle formation (NPF) (Elm, 2021; Hodshire et al., 2019). With
73 stringent global regulations reducing SO₂ emissions from fossil fuels (Perraud et al., 2015; Li et al., 2024b), MSA's
74 role in NPF has received widespread attention. Previous studies have investigated the effects of organic compounds
75 (HCOOH, CH₃COOH, CH₃OH, CH₂O, CH₃COCH₃, C₂H₅OC₂H₅, HCOOCH₃, H₂C₂O₄) (Zhao et al., 2017; Xu et
76 al., 2017a; Arquero et al., 2017; Xu et al., 2017b), iodic acid-containing (HIO₂, HIO₃) (Ning et al., 2022; Wu et al.,
77 2023c) and bases (NH₃, CH₃NH₂ (MA), (CH₃)₂NH, (CH₃)₃N) (Chen et al., 2016; Wen et al., 2018; Shen et al., 2020;
78 Liu et al., 2022) on MSA-driven binary nucleation, identifying MA as the most effective base in promoting MSA-
79 driven NPF. However, these binary nucleation mechanisms cannot fully explain the discrepancies observed between
80 measured and modeled global NPF rates, indicating the likely involvement of additional gaseous species (Lee et al.,
81 2019; Zhang et al., 2012). As a result, organic acids (Zhang et al., 2022) and inorganic acids (Hu et al., 2023) have
82 been proved to enhance the formation rate of MSA-MA-driven ternary nucleation in areas with abundant specific
83 pollutants. However, as one of the organic peroxides, the HMHP involved in MSA-MA-driven NPF remains
84 unexplored. This will limit our knowledge of frequent NPF events, especially in urban industrial areas and forested
85 areas.



86 In this work, the gaseous and interfacial formation mechanisms of HMHP catalyzed by MSA, as well as its
87 crucial role in MSA-MA nucleation, were explored. Specifically, quantum chemical calculations and Born-
88 Oppenheimer molecular dynamics (BOMD) simulations were employed to elucidate the reaction mechanism of
89 MSA-mediated CH₂OO hydrolysis leading to the formation of HMHP in both the gas phase and at the air-water
90 interface. Subsequently, the potential effect of HMHP in the MSA-MA-dominated NPF process was assessed under
91 a series of atmospheric conditions, utilizing quantum chemical calculation combined with the Atmospheric Cluster
92 Dynamics Code (ACDC). This work will not only enhances the understanding of HMHP formation but also
93 contributes to explaining some unexplained fluxes in NPF, while highlighting the significant impact of HMHP on
94 nucleation processes.

95 2. Methods

96 2.1 Quantum Chemical Calculations

97 To investigate the MSA-assisted CH₂OO hydrolysis in the gas phase, geometric configurations and vibrational
98 frequencies of all relevant configurations, including reactants, pre-reactive complexes, transition states (TSs), post-
99 reactive complexes, and products, were calculated at the M06-2X/6-311++G(2df,2pd) level (Mardirossian and
100 Head-Gordon, 2016; Pereira et al., 2017) using Gaussian 09. Intrinsic reaction coordinate analyses, performed at
101 the same computational level, verified the correspondence of each TS to its associated pre- and post-reactive
102 complexes. Subsequently, the ORCA software (Neese, 2012) was performed to compute the single point energies
103 using the CCSD(T)-F12/cc-pVDZ-F12 method.

104 To identify the global minimum energy configurations of (MSA)_x(MA)_y(HMHP)_z clusters, the ABCluster
105 program (Zhang and Dolg, 2015) was utilized to systematically generate initial configurations for various clusters.
106 Subsequently, these structures were further optimized using different levels of theoretical methods. Specifically, the
107 ABCluster program generated $n \times 1000$ ($1 < n \leq 4$) initial structures for each cluster system. Then, the PM6 semi-
108 empirical method (Partanen et al., 2016) was used for preliminary optimization of these structures. As the M06-2X
109 functional performs well for noncovalent binding and structural predictions of thermochemical and atmospheric
110 aggregates, 100 of the lowest-energy configurations were chosen from $n \times 1000$ ($1 < n \leq 3$) structures and re-
111 optimized using M06-2X/6-31G(d,p). Next, the 10 most stable configurations were re-optimized at the M06-2X/6-
112 311++G(2df,2pd) level, and the configuration with the lowest free energy was identified. Ultimately, single-point
113 energies were evaluated at the DLPNO-CCSD(T)-F12/cc-pVDZ-F12-CABS level (Tsona Tchinda et al., 2022) in
114 ORCA, using geometries optimized for the stable clusters at the M06-2X/6-311++G(2df,2pd) level.



115 **2.2 Rate coefficient calculations**

116 The rate coefficients of MSA-mediated CH₂OO hydrolysis were investigated through a two-step approach.
117 Initially, high-pressure-limit (HPL) rate coefficients were obtained using the VRC-VTST (Zhang et al., 2023; Zhang
118 et al., 2024) approach implemented in Polyrate 2017-C (Meana-Pañeda et al., 2024). Subsequently, MESMER
119 (Master Equation Solver for Multi-Energy Well Reactions) (Glowacki et al., 2012) was employed to calculate the
120 rate coefficients of MSA-catalyzed CH₂OO hydrolysis across the temperature range of 280.0-320.0 K. The rate
121 coefficients for the barrierless transition from separated reactants to pre-reactive complexes were estimated using
122 the Inverse Laplace Transform (ILT) (Kumar et al., 2021) method. Concurrently, RRKM theory was employed to
123 calculate the rate coefficients describing the conversion of the pre-reactive complex into the post-reactive species
124 through the transition state. Further descriptions of the ILT methods and RRKM theory are provided in Parts S1 and
125 S2 of the Supplement, respectively.

126 **2.3 Born-Oppenheimer Molecular Dynamic (BOMD) simulation**

127 BOMD calculations were carried out in CP2K program (Hutter et al., 2014), with exchange and correlation
128 interactions described by the BLYP functional (Becke, 1988). Dispersion effects were incorporated through
129 Grimme's dispersion (Grimme et al., 2010) (BLYP-D3) method. The Goedecker-Teter-Hutter (GTH) (Goedecker et
130 al., 1996) pseudopotential was adopted for the core region, whereas the valence electrons were represented through
131 a Gaussian DZVP basis (Phillips et al., 2005) in conjunction with an auxiliary plane-wave set. The calculations
132 employed a plane-wave energy cutoff of 280 Ry together with a 40 Ry cutoff for the Gaussian basis set. In the gas
133 phase, a supercell with a side length of 15 Å was employed to minimize periodic boundary effects, and the
134 integration was performed with a 0.5 fs timestep. A water droplet containing 191 molecules, serving as the interfacial
135 model, was subjected to BOMD pre-optimization for roughly 5.0 ps at 300 K. CH₂OO and MSA were then
136 positioned at the air-water interface, followed by 10 ps of molecular dynamics simulation. A supercell length of 35
137 Å was adopted to prevent interactions between periodic images of the droplet, while the dynamics were advanced
138 with a timestep of 1.0 fs. The gas-phase and interfacial simulations were conducted under NVT conditions at ~300
139 K, with the temperature maintained via a Nosé-Hoover thermostat.

140 **2.4 Atmospheric Clusters Dynamic Code (ACDC) Model**

141 ACDC (McGrath et al., 2012) was utilized to investigate the cluster formation rates, steady-state cluster
142 concentrations, and growth mechanisms within the extensive MSA-MA-HMHP system. Thermodynamic data,
143 calculated at the M06-2X/6-311++G(2df,2pd) level of theory, were employed as input parameters for the ACDC



144 simulations. The temporal progression of cluster concentrations was numerically resolved by solving the birth-death
145 equations, employing the ode15s solver within the MATLAB-R2013a program. The birth-death equations are given
146 below,

$$147 \quad \frac{dc_i}{dt} = \frac{1}{2} \sum_{j<i} \beta_{j,(i-j)} C_j C_{(i-j)} + \sum_j \gamma_{(i+j) \rightarrow i} C_{i+j} - \sum_j \beta_{i,j} C_i C_j - \frac{1}{2} \sum_{j<i} \gamma_{i \rightarrow j} C_i + Q_i - S_i \quad (1)$$

148 In this formulation, c_i denotes the concentration of cluster i , $\beta_{i,j}$ represents the collision coefficient of clusters i
149 with j and then $\gamma_{(i+j) \rightarrow i}$ represents the evaporation coefficient of clusters evaporating from $i+j$ to i and j clusters.
150 Q_i represents the potential source for cluster i , while S_i denotes the sink term for cluster i .

151 3. Results and discussion

152 3.1 The hydrolysis of CH₂OO with MSA in the gas phase

153 To evaluate the catalytic role of MSA in the CH₂OO hydrolysis reaction, the potential energy surface was
154 investigated both in the presence and absence of MSA and H₂O. As depicted in Fig. 1(a) and (b), the potential energy
155 surfaces with and without water closely match previously reported data (Wang et al., 2021a; Wang et al., 2021b),
156 suggesting that the CCSD(T)-F12/cc-pVDZ-F12//M06-2X/6-311++G(2df,2pd) method is suitable for assessing
157 MSA's catalytic effect. The MSA-catalyzed CH₂OO hydrolysis reaction (Fig. 1(c)) follows a continuous
158 bimolecular process, involving CH₂OO⋯H₂O + MSA and MSA⋯H₂O + CH₂OO. The stabilization energy of
159 MSA⋯H₂O is 9.8 kcal·mol⁻¹ higher than that of CH₂OO⋯H₂O. Considering the atmosphere concentrations of MSA
160 (Li et al., 2024b), H₂O (Anglada et al., 2013), and CH₂OO (Khan et al., 2018), the concentration of MSA⋯H₂O is
161 two orders of magnitude greater than that of CH₂OO⋯H₂O, predicting that the MSA⋯H₂O + CH₂OO route is the
162 dominant pathway for the MSA-catalyzed reaction. Starting from MSA⋯H₂O + CH₂OO, the reaction proceeds
163 through the IM_MSA intermediate, which has stabilization energy 6.5 kcal·mol⁻¹ and 0.7 kcal·mol⁻¹ higher than IM
164 and IM_WM, respectively. The increase in stabilization energy is primarily due to the addition of MSA, which
165 reduces ring strain and favours C-O bond formation. Atoms in Molecules (AIM) topological analysis results also
166 show that in IM_MSA ($\rho = 3.74 \times 10^{-2}$), the strength of the density of all electrons (C-O) is 1.64 times stronger than
167 in IM_WM ($\rho = 2.27 \times 10^{-2}$), further stabilizing the intermediate. The reaction then proceeds through the barrierless
168 transition state TS_MSA, forming a nine-membered ring complex HOCH₂OOH⋯MSA (labeled as IMF_MSA).
169 This process has a 1.4 kcal·mol⁻¹ lower energy barrier compared to the H₂O-catalyzed reaction, due to MSA's
170 enhanced ability to facilitate proton transfer. Additionally, IMF_MSA is more stable by 7.6 kcal·mol⁻¹ compared to
171 IMF_WM.



172 To further examine the impact of MSA on the CH₂OO hydrolysis reaction, we calculated the effective rate
173 constants for the CH₂OO hydrolysis assisted by H₂O ([H₂O] = 10¹⁵-10¹⁷ molecules·cm⁻³), NH₃ ([NH₃] = 10⁷-10¹¹
174 molecules·cm⁻³), H₂SO₄ ([H₂SO₄] = 10⁴-10⁸ molecules·cm⁻³) and MSA ([MSA] = 10⁴-10⁸ molecules·cm⁻³) in Table
175 S5. As H₂O concentrations in the atmosphere are much higher than those of MSA, the effective rate constants for
176 MSA-assisted CH₂OO hydrolysis were 4.04 × 10⁻²²-4.62 × 10⁻²³ cm³·molecule⁻¹·s⁻¹ when [MSA] = 10⁸
177 molecules·cm⁻³, which are 3-5 orders of magnitude smaller than the corresponding effective rate constants catalyzed
178 by H₂O ([H₂O] = 10¹⁵-10¹⁷ molecules·cm⁻³) at 298.15 K. However, when [MSA] = 10⁶-10⁸ molecules·cm⁻³, the
179 catalytic effect of MSA was significantly more favorable than that of NH₃ ([NH₃] = 10⁷-10¹¹ molecules·cm⁻³) with
180 k'_{MSA} being larger by about 2-6 orders of magnitude within the temperature range of 280.0-320.0 K. Meanwhile,
181 when the concentration of [MSA] range from 10⁵ to 10⁸ molecules·cm⁻³, it has been observed that MSA exhibits
182 significantly greater catalytic ability compared to SA ([SA] = 10⁴-10⁷ molecules·cm⁻³). Specifically, the effective
183 rate constant, k'_{MSA} is approximately 1 to 3 orders of magnitude higher than k'_{SA} .

184 3.2 The hydrolysis of CH₂OO with MSA at the air-water interface

185 The mechanism of MSA-catalyzed CH₂OO hydrolysis at the air-water interface remained unclear. To elucidate
186 this process, BOMD simulations were employed to investigate possible reaction pathways at the aqueous interface.
187 Based on analogies with CH₂OO reactions involving other atmospheric species (Ding et al., 2024; Li et al., 2023;
188 Cheng et al., 2025), three potential routes were considered: (i) MSA interacting with adsorbed CH₂OO at the air-
189 water interface, (ii) CH₂OO interacting with adsorbed MSA at the air-water interface, or (iii) the MSA-CH₂OO
190 complex reacting at the air-water interface. Because both CH₂OO and MSA exhibit high reactivity toward interfacial
191 water, their lifetimes at the droplet interface remain very brief, making pathway (i) and (ii) far less likely than
192 pathway (iii). Therefore, only the reaction of the MSA···CH₂OO complex at the aqueous interface was considered,
193 owing to its high stability in the gas phase.

194 As displayed in Fig. 2, Fig. S1, and Movie S1, the MSA···CH₂OO complex initially interacts with a water
195 molecule at the aqueous interface. At 0.76 ps, this water molecule forms both a van der Waals interaction with the
196 carbon atom in CH₂OO (d(C-O3) = 4.00 Å) and a hydrogen bond with the oxygen atom in MSA (d(O4-H2) = 3.27
197 Å), thereby generating a nine-membered ring structure (CH₂OO···MSA···H₂O). As the reaction progresses, a
198 hydration transition-state-like ring configuration forms at 1.06 ps, with the C-O3, O4-H2 and O2-H1 bonds shorten
199 to 1.75 Å, 1.27 Å and 0.97 Å, respectively, while the O3-H2 and O1-H1 bonds elongate to 1.16 Å and 1.85 Å,
200 respectively. By 1.16 ps, the bond lengths of C-O3, O4-H2 and O2-H1 further shorten to 1.43 Å, 1.05 Å and 0.96



201 Å, while the O3-H2 and O1-H1 bonds further increase to 1.61 Å and 1.93 Å, respectively, indicating the formation
202 of the hydrogen-bonded CH₂OOHOH...MSA complex. During this process, the interfacial water molecule acts as a
203 reactant, with MSA serving as a proton transfer bridge. Notably, due to the higher abundance of interfacial water
204 molecules compared to MSA, the formation of HMHP at the interface primarily proceeds through the direct
205 hydration of CH₂OO. However, the source of HMHP from MSA-catalyzed CH₂OO hydrolysis at the interface occurs
206 at a significantly faster rate than its corresponding gas-phase formation, with a computed ratio (r_1) of 1.01×10^2 at
207 298.0 K, which is detailed computational results are provided in Part S3. Traditionally, the loss of CH₂OO in the
208 troposphere has been primarily attributed to its hydrolysis. Therefore, it is crucial to examine the rate ratio r_2
209 (equation (S4)) between interfacial MSA-catalyzed CH₂OO hydrolysis and the corresponding gas-phase process
210 mediated by water. At 298.0 K, r_2 is 13.4, indicating that the formation of HMHP from interfacial MSA-mediated
211 CH₂OO hydrolysis is much closer to that catalyzed by water in the gas phase. These results indicate that interfacial
212 MSA-catalyzed CH₂OO hydrolysis is a significant source of HMHP formation in MSA-polluted areas under
213 relatively humid conditions. Consequently, when evaluating the comprehensive sources of HMHP in MSA-rich
214 regions, it is essential to consider the formation involving MSA-catalyzed hydrolysis of CH₂OO at the air-water
215 interface.

216 3.3 The significance of HMHP in MSA-MA nucleation

217 The role of HMHP on MSA-MA-driven ternary nucleation was assessed. Initial assessments focused on the
218 potential interaction sites of HMHP with MSA and MA, followed by an analysis of the conformation and stability
219 of the (MSA)_x(MA)_y(HMHP)_z ($0 \leq y \leq x + z \leq 3$) clusters. The MSA-MA nucleation mechanism involving
220 HMHP was then examined, along with the effects of temperature and precursor concentrations on the MSA-MA-
221 HMHP system. Finally, the atmospheric implication of HMHP for MSA-MA nucleation were calculated for urban
222 industrial areas and forested areas.

223 3.3.1 Cluster conformational analysis

224 The formation of stable clusters is primarily dictated by the pronounced coupling of nucleation precursors
225 (Ning et al., 2024; Li et al., 2024a; Li et al., 2024b). The electrostatic potential (ESP)-mapped molecular van der
226 Waals (vdW) surface was computed to characterize the binding potential of HMHP with MSA and MA and to locate
227 the corresponding interaction sites (Fig. 3(a)). The analysis revealed that HMHP exhibits a positive ESP value
228 (+54.09 kcal·mol⁻¹) at the H atom of its -OH group, indicating its role as a hydrogen bond (HB) donor, while the
229 oxygen atom of the -COOH shows a negative ESP of -32.68 kcal·mol⁻¹, indicating its role as a hydrogen bond



230 acceptor. Thus, HMHP possesses dual functionalities as a HB donor and acceptor, allowing its association with the
231 nucleating precursors MSA and MA, thereby generating HBs that stabilize the MSA-MA-HMHP clusters. Based
232 on the ESP analysis, the most stable configurations of $(MSA)_x(MA)_y(HMHP)_z$ clusters were obtained (Fig. S2), and
233 the actual binding sites within the ternary clusters were found to be consistent with the predictions from the ESP
234 analysis.

235 To further access the non-covalent interactions within the $(MSA)_x(MA)_y(HMHP)_z$ clusters, the reduced density
236 gradient (RDG) analysis was performed on representative clusters, including $(MSA)_1 \cdot (MA)_1$,
237 $(MSA)_1 \cdot (MA)_1 \cdot (HMHP)_1$ and $(MSA)_1 \cdot (MA)_1 \cdot (HMHP)_2$ cluster (Fig. 3(b)). In the RDG analysis, the blue region
238 corresponds to strong attractions, similar to HBs, within the system. When compared to the $(MSA)_1 \cdot (MA)_1$ cluster,
239 the $(MSA)_1 \cdot (MA)_1 \cdot (HMHP)_1$ cluster exhibits two additional blue spikes, suggesting that HMHP forms strong
240 interactions, particularly HBs, with MSA and MA. Moreover, the dominant blue spike in the
241 $(MSA)_1 \cdot (MA)_1 \cdot (HMHP)_2$ cluster is shifted further leftward compared to that in the $(MSA)_1 \cdot (MA)_1 \cdot (HMHP)_1$ cluster,
242 indicating the introduction of HMHP molecules strengthens the HB interactions within the system. Besides, in
243 clusters involving HMHP (Fig. S2), HMHP facilitates the formation of cage-like clusters with MSA and MA through
244 a spatial network of HBs. Notably, proton transfer is observed in ternary clusters involving HMHP. Taken together,
245 these findings suggest that HMHP forms stable clusters with MSA and MA via both HBs and proton transfer, thereby
246 enhancing the stability of the MSA-MA-HMHP clusters.

247 3.3.2 Cluster stability analysis

248 To prove the enhancing effect of HMHP on the thermodynamic stability of MSA-MA-clusters, the Gibbs free
249 energy (Fig. 4) and total evaporation rates (Table S10) associated with cluster in the MSA-MA-HMHP system were
250 calculated. Fig. 4 illustrates that the cluster growth pathway of the MSA-MA-HMHP system, established from Gibbs
251 free energy calculations, can be classified into two main categories: (i) non-HMHP pathways, involving MSA-MA
252 nucleation and (ii) HMHP-involved pathways, including MSA-MA-HMHP nucleation. For the pure MSA-MA
253 nucleation route, the generation of the heterodimer $(MSA)_1 \cdot (MA)_1$ proceeds barrierlessly. The predominant growth
254 pathway subsequently follows the low-energy route, characterized by the incorporation of a single MSA or MA
255 molecule. Within the MSA-MA-HMHP system, the evolution from $(MSA)_1 \cdot (MA)_1$ to $(MSA)_1 \cdot (MA)_1 \cdot (HMHP)_1$
256 occurs without an energy barrier. Furthermore, once the $(MSA)_1 \cdot (MA)_1 \cdot (HMHP)_1$ cluster is formed, the continue
257 collision with MSA or MA monomer also proceeds through a barrierless clustering process, primarily resulting in
258 the growth of stable clusters, including $(MSA)_2 \cdot (MA)_1 \cdot (HMHP)_1$, $(MSA)_2 \cdot (MA)_2 \cdot (HMHP)_1$ and



259 $(\text{MSA})_2 \cdot (\text{MA})_3 \cdot (\text{HMHP})_1$. Notably, the $(\text{MSA})_1 \cdot (\text{MA})_1 \cdot (\text{HMHP})_1$ and $(\text{MSA})_2 \cdot (\text{MA})_2 \cdot (\text{HMHP})_1$ clusters exhibited
260 Gibbs free energies that were 10.66 kcal·mol⁻¹ and 10.24 kcal·mol⁻¹ lower than those of the corresponding
261 $(\text{MSA})_1 \cdot (\text{MA})_1$ and $(\text{MSA})_2 \cdot (\text{MA})_2$ clusters. Simultaneously, MSA-MA-HMHP clusters enriched with HMHP
262 exhibited total evaporation rates lower than those of the corresponding MSA-MA clusters. Overall, these analyses
263 of Gibbs free energies and total evaporation rates provide strong evidence that HMHP molecules contribute to the
264 stabilization of MSA-MA cluster formation. This suggests that HMHP molecules are likely participate in the
265 nucleation process of the MSA-MA clusters.

266 3.3.3 Cluster formation pathways

267 To track the detailed nucleation pathways of HMHP involved in the formation of MSA-MA clusters, ACDC
268 simulation were conducted at three different temperatures (238.15 K, 258.15 K and 278.15 K), with concentrations
269 set as $[\text{MSA}] = 1.0 \times 10^6$ molecules·cm⁻³, $[\text{MA}] = 2.5 \times 10^8$ molecules·cm⁻³ and $[\text{HMHP}] = 1.0 \times 10^{11}$ molecules·cm⁻³.
270 The results are presented in Fig. 5(a). At 238.15 K, the primary growth of the MSA-MA-HMHP system can be
271 divided into two distinct routes. One pathway involves MSA-MA clustering alone, while the other incorporates
272 HMHP molecules in the cluster formation process. In the HMHP involving pathway, HMHP initially interacts with
273 the heterodimer $(\text{MSA})_2 \cdot (\text{MA})_2$, resulting in the formation of a $(\text{MSA})_2 \cdot (\text{MA})_2 \cdot (\text{HMHP})$ trimer. This trimer then
274 grows out of the simulated system. Following this, the $(\text{MSA})_2 \cdot (\text{MA})_2 \cdot (\text{HMHP})$ trimer collides with an MSA
275 monomer, forming the cluster $(\text{MSA})_3 \cdot (\text{MA})_2 \cdot (\text{HMHP})$. Subsequently, HMHP evaporates from this cluster, leaving
276 behind the $(\text{MSA})_3 \cdot (\text{MA})_2$ cluster. Finally, the $(\text{MSA})_3 \cdot (\text{MA})_2$ trimer interacts with an MA monomer, resulting in
277 the $(\text{MSA})_3 \cdot (\text{MA})_3$ cluster, which eventually exits the system. These processes illustrate HMHP's dual function: it
278 acts both as a “catalyst” that promotes the formation of MSA-MA clusters and as a “participant” in the assembly of
279 critical clusters. This dual role is also observed at 258.15 K. However, at 278.15 K, HMHP functions solely as a
280 “participant” in the formation of critical clusters. The higher evaporation coefficient of clusters at elevated
281 temperatures leads to their faster evaporation. Together, these findings underscore the significant and direct role of
282 HMHP in MSA-MA nucleation, effectively facilitating cluster formation across different temperatures.

283 To further investigate the influence of temperature (T) on HMHP's participation role in the MSA-MA
284 nucleation process, we analyzed the contribution of different clustering pathways to the outward flux under varying
285 T . As shown in Fig. 5(b), with increasing T , the dominance of HMHP-involved pathways gradually diminishes. At
286 238.15-258.15 K, the HMHP-involved pathway accounts for 63%, whereas at 278.15 K, the contribution decreases
287 to 21%. These results highlight the significant role of low temperatures in facilitating HMHP's participation in



288 MSA-MA nucleation. In addition to T , the contribution of nucleating precursor flux also significantly affects trace
289 substances' involvement in the MSA-MA nucleation process. The contribution of HMHP to the MSA-MA system
290 was found to be relatively insensitive to $[MA]$, as illustrated in Fig. S3. In contrast, it is strongly influenced by
291 $[MSA]$, as depicted in Fig. 5(c). As $[MSA]$ increases from 10^4 to 10^8 molecules·cm⁻³, the contribution of HMHP-
292 involved pathways decreases from 65% to 40%. At the low $[MSA]$ (10^4 - 10^6 molecules·cm⁻³), HMHP involvement
293 remains substantial, accounting for 65% of the pathway. Overall, this study reveals that HMHP's contribution to
294 MSA-MA nucleation is most pronounced under conditions of low T , and low concentrations of both MSA and MA.

295 3.4 Atmospheric implications of HMHP to MSA-MA system

296 Building on the above findings, low T coupled with low $[MSA]$ and $[MA]$ appear to favor an enhanced role of
297 HMHP in MSA-MA nucleation. To assess the atmospheric significance of these variations, we quantified the
298 contributions of MSA-MA cluster growth pathways, with and without HMHP involvement (Fig. 6), under favorable
299 conditions of temperature ($T = 258.15$ K) and precursor concentrations ($[MSA] = 1.00 \times 10^4$ molecules·cm⁻³, $[MA]$
300 $= 2.50 \times 10^7$ molecules·cm⁻³). Indeed, substantial variability in atmospheric HMHP concentrations has been
301 observed across diverse environments worldwide. For example, levels range from 2.50×10^9 to 6.25×10^9
302 molecules·cm⁻³ in Central Portugal, Pabstthum, and Beijing. Higher concentrations, between 1.15×10^{10} to $3.00 \times$
303 10^{10} molecules·cm⁻³, have been observed in Guang Zhou and Niwot Ridge, while the forests of the Southeastern
304 United States exhibit the highest concentrations, reaching up to 1.25×10^{11} molecules·cm⁻³. As shown in Fig. 6, in
305 low $[HMHP]$ regions such as Pabstthum and Beijing, HMHP-involved pathways account for only 11% and 12% of
306 total NPF, respectively. In contrast, in high $[HMHP]$ environments, including the Southeastern United States (1.25
307 $\times 10^{11}$ molecules·cm⁻³) and Niwot Ridge (3.00×10^{10} molecules·cm⁻³), these contributions increase sharply to 59%
308 and 42%, respectively. These results highlight that HMHP exerts a markedly stronger influence on MSA-MA
309 nucleation at elevated concentrations, particularly in urban–industrial and forested regions, where its contribution
310 to NPF can be substantial.

311 4. Conclusions

312 The hydrolysis of CH₂OO by MSA, occurring in both the gas phase and at interfaces and resulting in
313 hydroxymethyl hydroperoxide (HMHP) formation, was investigated. In addition, the role of HMHP in promoting
314 MSA-MA nucleation was elucidated.

315 Quantum chemical calculations suggest that the activation energy for HMHP formation via MSA-catalyzed
316 gaseous hydrolysis of CH₂OO is relatively low, observed to be 2.9 kcal mol⁻¹. At a concentration of $[MSA] = 10^6$ -



317 10^8 molecules·cm⁻³, MSA exhibits a dominant catalytic effect compared to other catalysts, such as NH₃ ([NH₃] =
318 10^7 - 10^{11} molecules·cm⁻³), within the temperature range of 280.0-320.0 K. Notably, the computed effective rate
319 constant for MSA is larger by about 2-6 orders of magnitude compared with that of NH₃. Simultaneously, when
320 [MSA] = 10^5 - 10^8 molecules·cm⁻³, k'_{MSA} is found to be 1 to 3 orders of magnitude larger than k'_{SA} , which corresponds
321 to [SA] = 10^4 - 10^7 molecules·cm⁻³. BOMD simulations further demonstrate that the MSA-catalyzed CH₂OO
322 hydrolysis at the gas-liquid interface follows a ring-based reaction mechanism on a picosecond timescale.
323 Remarkably, HMHP formation through MSA-catalyzed CH₂OO hydrolysis occurs rapidly and stably at the interface.

324 HMHP participates in MSA-MA-driven ternary nucleation through its bifunctional hydrogen-bonding capacity,
325 which allows direct association with both MSA and MA. Thermodynamic analysis shows that MSA-MA-HMHP
326 trimers possess lower Gibbs free energy than MSA-MA dimers, indicating enhanced cluster stability. Cluster
327 formation pathways analysis reveals a temperature-dependent role: at 238.15 K and 258.15 K, HMHP functions as
328 both catalyst and participant, whereas at 278.15 K it acts solely as a participant due to increased evaporation rates.
329 Under low temperature, low [MSA] and [MA], and high [HMHP] conditions, particularly in Niwot Ridge and the
330 southeastern United States, HMHP-involved pathways contribute up to 59% and 42% of total nucleation flux. These
331 results predict that HMHP substantially enhances MSA-MA-driven NPF in urban industrial and forested regions,
332 helping to explain previously unaccounted NPF sources and improve nucleation models.

333 Overall, this work deepens the understanding of hydroperoxide formation in MSA-polluted regions, especially
334 at the gas-liquid interface. It also reveals the potential contribution of other organic peroxides to NPF, offering a
335 plausible explanation for part of the unaccounted particle fluxes in both urban industrial and forested regions.

336 **Data availability**

337 Data will be made available on request.

338 **Authorship contributions**

339 RL: methodology, investigation, data curation, writing (original draft). ZL: writing (review), data curation,
340 methodology, investigation. CZ: writing (review), data computation. JY: data curation, data computation. HC:
341 writing (editing), data curation, visualization, investigation. XL: writing (review and editing). NH: data curation,
342 project administration, writing (review and editing). RW: funding acquisition, writing (review and editing). TZ:
343 writing (review and editing), funding acquisition.

344 **Competing interests**



345 The authors declare that they have no known competing financial interests or personal relationships that could
346 have appeared to influence the work reported in this paper.

347 Acknowledgements

348 This work was supported by the National Natural Science Foundation of China (No: 22203052; 22073059),
349 the Funds of Graduate Innovation of Shaanxi University of Technology (No: SLGYCX2506).

350 References

- 351 Allen, H. M., Crounse, J. D., Bates, K. H., Teng, A. P., Krawiec-Thayer, M. P., Rivera-Rios, J. C., Keutsch, F. N., St. Clair,
352 J. M., Hanisco, T. F., Möller, K. H., Kjaergaard, H. G., and Wennberg, P. O.: Kinetics and Product Yields of the OH
353 Initiated Oxidation of Hydroxymethyl Hydroperoxide, *J. Phys. Chem. A*, 122, 6292-6302,
354 <https://doi.org/10.1021/acs.jpca.8b04577>, 2018.
- 355 Anglada, J. M., Hoffman, G. J., Slipchenko, L. V., M.Costa, M., Ruiz-López, M. F., and Francisco, J. S.: Atmospheric
356 Significance of Water Clusters and Ozone-Water Complexes, *J. Phys. Chem. A*, 117, 10381-10396,
357 <https://doi.org/10.1021/jp407282c>, 2013.
- 358 Anglada, J. M., and Solé, A.: Impact of the water dimer on the atmospheric reactivity of carbonyl oxides, *Phys. Chem.*
359 *Chem. Phys.*, 18, 17698-17712, <https://doi.org/10.1039/C6CP02531E>, 2016.
- 360 Arquero, K. D., Gerber, R. B., and Finlayson-Pitts, B. J.: The Role of Oxalic Acid in New Particle Formation from
361 Methanesulfonic Acid, Methylamine, and Water, *Environ. Sci. Technol.*, 51, 2124-2130,
362 <https://doi.org/10.1021/acs.est.6b05056>, 2017.
- 363 Becke, A. D.: Density-functional exchange-energy approximation with correct asymptotic behavior, *Phys. Rev. A*, 38,
364 3098-3100, <https://doi.org/10.1103/PhysRevA.38.3098>, 1988.
- 365 Berndt, T., Kaethner, R., Voigtländer, J., Stratmann, F., Pfeifle, M., Reichle, P., Sipilä, M., Kulmala, M., and Olzmann,
366 M.: Kinetics of the unimolecular reaction of CH₂OO and the bimolecular reactions with the water monomer,
367 acetaldehyde and acetone under atmospheric conditions, *Phys. Chem. Chem. Phys.*, 17, 19862-19873,
368 <https://doi.org/10.1039/C5CP02224J>, 2015.
- 369 Chao, W., Hsieh, J.-T., Chang, C.-H., and Lin, J. J.-M.: Direct kinetic measurement of the reaction of the simplest
370 Criegee intermediate with water vapor, *Science*, 347, 751-754, <https://doi.org/10.1126/science.1261549>, 2015.
- 371 Chao, W., Yin, C., Takahashi, K., and Lin, J. J.-M.: Effects of water vapor on the reaction of CH₂OO with NH₃, *Phys.*
372 *Chem. Chem. Phys.*, 21, 22589-22597, <https://doi.org/10.1039/C9CP04682H>, 2019.
- 373 Chen, H., Varner, M. E., Gerber, R. B., and Finlayson-Pitts, B. J.: Reactions of Methanesulfonic Acid with Amines and
374 Ammonia as a Source of New Particles in Air, *J. Phys. Chem. B*, 120, 1526-1536,
375 <https://doi.org/10.1021/acs.jpcc.5b07433>, 2016.
- 376 Cheng, Y., Ding, C., Zhang, T., Wang, R., Mu, R., Li, Z., Li, R., Shi, J., and Zhu, C.: Barrierless reactions of C₂ Criegee
377 intermediates with H₂SO₄ and their implication to oligomers and new particle formation, *J. Environ. Sci.*, 149, 574-
378 584, <https://doi.org/10.1016/j.jes.2023.12.020>, 2025.
- 379 Ding, C., Wen, M., Zhang, T., Li, Z., Li, R., Wang, R., Ou, T., Song, F., and Zhang, Q.: Molecular mechanisms and
380 atmospheric implications of the simplest criegee intermediate and hydrochloric acid chemistry in the gas phase and
381 at the aqueous interfaces, *Atmos. Environ.*, 330, 120558, <https://doi.org/10.1016/j.atmosenv.2024.120558>, 2024.
- 382 Dong, Z., Francisco, J. S., and Long, B.: Ammonolysis of Glyoxal at the Air-Water Nanodroplet Interface, *Angew. Chem.*
383 *Int. Ed.*, 63, e202316060, <https://doi.org/10.1002/anie.202316060>, 2024.



- 384 Elm, J.: Clusteromics II: Methanesulfonic Acid-Base Cluster Formation, *ACS omega*, 6, 17035-17044,
385 <https://doi.org/10.1021/acsomega.1c02115>, 2021.
- 386 Fang, Y.-G., Wei, L., Francisco, J. S., Zhu, C., and Fang, W.-H.: Mechanistic Insights into Chloric Acid Production by
387 Hydrolysis of Chlorine Trioxide at an Air-Water Interface, *J. Am. Chem. Soc.*, 146, 21052-21060,
388 <https://doi.org/10.1021/jacs.4c06269>, 2024.
- 389 Glowacki, D. R., Liang, C.-H., Morley, C., Pilling, M. J., and Robertson, S. H.: MESMER: An Open-Source Master
390 Equation Solver for Multi-Energy Well Reactions, *J. Phys. Chem. A*, 116, 9545-9560,
391 <https://doi.org/10.1021/jp3051033>, 2012.
- 392 Goedecker, S., Teter, M., and Hutter, J.: Separable dual-space Gaussian pseudopotentials, *Phys. Rev. B*, 54, 1703-1710,
393 <https://doi.org/10.1103/PhysRevB.54.1703>, 1996.
- 394 Grimme, S., Antony, J., Ehrlich, S., and Krieg, H.: A consistent and accurate ab initio parametrization of density functional
395 dispersion correction (DFT-D) for the 94 elements H-Pu, *J. Chem. Phys.*, 132, <https://doi.org/10.1063/1.3382344>,
396 2010.
- 397 Grossmann, D., Moortgat, G. K., Kibler, M., Schlomski, S., Bächmann, K., Alicke, B., Geyer, A., Platt, U., Hammer,
398 M.-U., Vogel, B., Mihelcic, D., Hofzumahaus, A., Holland, F., and Volz-Thomas, A.: Hydrogen peroxide,
399 organic peroxides, carbonyl compounds, and organic acids measured at Pabstthum during BERLIOZ, *J.*
400 *Geophys. Res. Atmos.*, 108, <https://doi.org/10.1029/2001JD001096>, 2003.
- 401 Hewitt, C. N., and Kok, G. L.: Formation and occurrence of organic hydroperoxides in the troposphere: Laboratory and
402 field observations, *J. Atmos. Chem.*, 12, 181-194, <https://link.springer.com/article/10.1007/BF00115779>, 1991.
- 403 Hodshire, A. L., Campuzano-Jost, P., Kodros, J. K., Croft, B., Nault, B. A., Schroder, J. C., Jimenez, J. L., and Pierce, J.
404 R.: The potential role of methanesulfonic acid (MSA) in aerosol formation and growth and the associated radiative
405 forcings, *Atmos. Chem. Phys.*, 19, 3137-3160, <https://doi.org/10.5194/acp-19-3137-2019>, 2019.
- 406 Hu, Y., Chen, S., Ye, S., Wei, S., Chu, B., Wang, R., Li, H., and Zhang, T.: The role of trifluoroacetic acid in new particle
407 formation from methanesulfonic acid-methylamine, *Atmos. Environ.*, 311, 120001,
408 <https://doi.org/10.1016/j.atmosenv.2023.120001>, 2023.
- 409 Hutter, J., Iannuzzi, M., Schiffmann, F., and VandeVondele, J.: cp2k: atomistic simulations of condensed matter
410 systems, *WIREs Comput. Mol. Sci.*, 4, 15-25, <https://doi.org/10.1002/wcms.1159>, 2014.
- 411 Jackson, A. V., and Hewitt, C. N.: Hydrogen peroxide and organic hydroperoxide concentrations in air in a eucalyptus
412 forest in central Portugal, *Atmos. Environ.*, 30, 819-830, [https://doi.org/10.1016/1352-2310\(95\)00348-7](https://doi.org/10.1016/1352-2310(95)00348-7), 1996.
- 413 Khan, M. A. H., Percival, C. J., Caravan, R. L., Taatjes, C. A., and Shallcross, D. E.: Criegee intermediates and their
414 impacts on the troposphere, *Environ. Sci.: Processes Impacts*, 20, 437-453, <https://doi.org/10.1039/C7EM00585G>,
415 2018.
- 416 Kumar, A., Mallick, S., and Kumar, P.: Oxidation of HOSO' by Cl': a new source of SO₂ in the atmosphere?, *Phys.*
417 *Chem. Chem. Phys.*, 23, 18707-18711, <https://doi.org/10.1039/D1CP01048D>, 2021.
- 418 Lee, J. H., Leahy, D. F., Tang, I. N., and Newman, L.: Measurement and speciation of gas phase peroxides in the
419 atmosphere, *J. Geophys. Res. Atmos.*, 98, 2911-2915, <https://doi.org/10.1029/92JD02514>, 1993.
- 420 Lee, S.-H., Gordon, H., Yu, H., Lehtipalo, K., Haley, R., Li, Y., and Zhang, R.: New Particle Formation in the
421 Atmosphere: From Molecular Clusters to Global Climate, *J. Geophys. Res. Atmos.*, 124, 7098-7146,
422 <https://doi.org/10.1029/2018JD029356>, 2019.
- 423 Li, J., Ning, A., Liu, L., and Zhang, X.: Atmospheric Bases-Enhanced Iodic Acid Nucleation: Altitude-Dependent
424 Characteristics and Molecular Mechanisms, *Environ. Sci. Technol.*, 58, 16962-16973,
425 <https://doi.org/10.1021/acs.est.4c06053>, 2024a.
- 426 Li, J., Wu, N., Chu, B., Ning, A., and Zhang, X.: Molecular-level study on the role of methanesulfonic acid in iodine
427 oxoacid nucleation, *Atmos. Chem. Phys.*, 24, 3989-4000, <https://doi.org/10.5194/acp-24-3989-2024>, 2024b.



- 428 Li, L., Zhang, Q., Wei, Y., Wang, Q., and Wang, W.: Theoretical Study on the Gas Phase and Gas-Liquid Interface Reaction
429 Mechanism of Criegee Intermediates with Glycolic Acid Sulfate, *Int. J. Mol. Sci.*, 24, 3355,
430 <https://doi.org/10.3390/ijms24043355>, 2023.
- 431 Li, M., Li, L., Liu, S., Zhang, Q., Wang, W., and Wang, Q.: Insights into the catalytic effect of atmospheric organic
432 trace species on the hydration of Criegee intermediates, *Sci. Total Environ.*, 949, 174877,
433 <https://doi.org/10.1016/j.scitotenv.2024.174877>, 2024c.
- 434 Lin, L.-C., Chang, H.-T., Chang, C.-H., Chao, W., Smith, M. C., Chang, C.-H., Jr-Min Lin, J., and Takahashi, K.:
435 Competition between H₂O and (H₂O)₂ reactions with CH₂OO/CH₃CHOO, *Phys. Chem. Chem. Phys.*, 18, 4557-4568,
436 <https://doi.org/10.1039/C5CP06446E>, 2016.
- 437 Liu, Y., Xie, H.-B., Ma, F., Chen, J., and Elm, J.: Amine-Enhanced Methanesulfonic Acid-Driven Nucleation: Predictive
438 Model and Cluster Formation Mechanism, *Environ. Sci. Technol.*, 56, 7751-7760,
439 <https://doi.org/10.1021/acs.est.2c01639>, 2022.
- 440 Long, B., Bao, J. L., and Truhlar, D. G.: Atmospheric Chemistry of Criegee Intermediates: Unimolecular Reactions and
441 Reactions with Water, *J. Am. Chem. Soc.*, 138, 14409-14422, <https://doi.org/10.1021/jacs.6b08655>, 2016.
- 442 Mardirossian, N., and Head-Gordon, M.: How Accurate Are the Minnesota Density Functionals for Noncovalent
443 Interactions, Isomerization Energies, Thermochemistry, and Barrier Heights Involving Molecules Composed of
444 Main-Group Elements?, *J. Chem. Theory Comput.*, 12, 4303-4325, <https://doi.org/10.1021/acs.jctc.6b00637>, 2016.
- 445 McGrath, M. J., Olenius, T., Ortega, I. K., Loukonen, V., Paasonen, P., Kurtén, T., Kulmala, M., and Vehkamäki, H.:
446 Atmospheric Cluster Dynamics Code: a flexible method for solution of the birth-death equations, *Atmos. Chem.*
447 *Phys.*, 12, 2345-2355, <https://doi.org/10.5194/acp-12-2345-2012>, 2012.
- 448 Meana-Pañeda, R., Zheng, J., Bao, J. L., Zhang, S., Lynch, B. J., Corchado, J. C., Chuang, Y.-Y., Fast, P. L., Hu,
449 W.-P., Liu, Y.-P., Lynch, G. C., Nguyen, K. A., Jackels, C. F., Fernández-Ramos, A., Ellingson, B. A., Melissas,
450 V. S., Villà, J., Rossi, I., Coitiño, E. L., Pu, J., Albu, T. V., Zhang, R. M., Xu, X., Ratkiewicz, A., Steckler, R.,
451 Garrett, B. C., Isaacson, A. D., and Truhlar, D. G.: Polyrate 2023: A computer program for the calculation of
452 chemical reaction rates for polyatomics. New version announcement, *Comput. Phys. Commun.*, 294, 108933,
453 <https://doi.org/10.1016/j.cpc.2023.108933>, 2024.
- 454 Neese, F.: The ORCA program system, *Mol. Sci.*, 2, 73-78, <https://doi.org/10.1002/wcms.81>, 2012.
- 455 Newland, M. J., Rickard, A. R., Vereecken, L., Muñoz, A., Ródenas, M., and Bloss, W. J.: Atmospheric isoprene
456 ozonolysis: impacts of stabilised Criegee intermediate reactions with SO₂, H₂O and dimethyl sulfide, *Atmos.*
457 *Chem. Phys.*, 15, 9521-9536, <https://doi.org/10.5194/acp-15-9521-2015>, 2015.
- 458 Nguyen, T. B., Crouse, J. D., Teng, A. P., St. Clair, J. M., Paulot, F., Wolfe, G. M., and Wennberg, P. O.: Rapid deposition
459 of oxidized biogenic compounds to a temperate forest, *Proc. Natl. Acad. Sci. U.S.A.*, 112, E392-E401,
460 <https://doi.org/10.1073/pnas.1418702112>, 2015.
- 461 Ning, A., Liu, L., Ji, L., and Zhang, X.: Molecular-level nucleation mechanism of iodic acid and methanesulfonic acid,
462 *Atmos. Chem. Phys.*, 22, 6103-6114, <https://doi.org/10.5194/acp-22-6103-2022>, 2022.
- 463 Ning, A., Shen, J., Zhao, B., Wang, S., Cai, R., Jiang, J., Yan, C., Fu, X., Zhang, Y., Li, J., Ouyang, D., Sun, Y., Saiz-
464 Lopez, A., Francisco, J. S., and Zhang, X.: Overlooked significance of iodic acid in new particle formation in
465 the continental atmosphere, *Proc. Natl. Acad. Sci. U.S.A.*, 121, e2404595121,
466 <https://doi.org/10.1073/pnas.2404595121>, 2024.
- 467 Ouyang, B., McLeod, M. W., Jones, R. L., and Bloss, W. J.: NO₃ radical production from the reaction between the Criegee
468 intermediate CH₂OO and NO₂, *Phys. Chem. Chem. Phys.*, 15, 17070-17075, <https://doi.org/10.1039/C3CP53024H>,
469 2013.



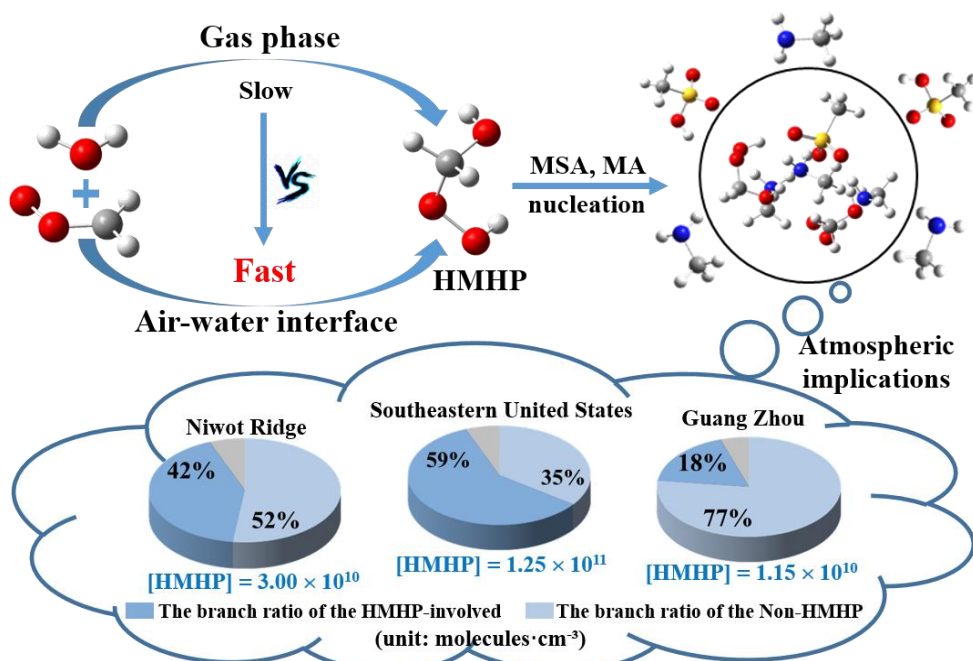
- 470 Partanen, L., Vehkamäki, H., Hansen, K., Elm, J., Henschel, H., Kurtén, T., Halonen, R., and Zapadinsky, E.: Effect of
471 Conformers on Free Energies of Atmospheric Complexes, *J. Phys. Chem. A*, 120, 8613-8624,
472 <https://doi.org/10.1021/acs.jpca.6b04452>, 2016.
- 473 Pereira, A. T., Ribeiro, A. J. M., Fernandes, P. A., and Ramos, M. J.: Benchmarking of density functionals for the
474 kinetics and thermodynamics of the hydrolysis of glycosidic bonds catalyzed by glycosidases, *Int. J. Quantum*
475 *Chem.*, 117, e25409, <https://doi.org/10.1002/qua.25409>, 2017.
- 476 Perraud, V., Horne, J. R., Martinez, A. S., Kalinowski, J., Meinardi, S., Dawson, M. L., Wingen, L. M., Dabdub, D., Blake,
477 D. R., Gerber, R. B., and Finlayson-Pitts, B. J.: The future of airborne sulfur-containing particles in the absence of
478 fossil fuel sulfur dioxide emissions, *Proc. Natl. Acad. Sci. U.S.A.*, 112, 13514-13519,
479 <https://doi.org/10.1073/pnas.1510743112>, 2015.
- 480 Phillips, J. C., Braun, R., Wang, W., Gumbart, J., Tajkhorshid, E., Villa, E., Chipot, C., Skeel, R. D., Kalé, L., and
481 Schulten, K.: Scalable molecular dynamics with NAMD, *J. Comput Chem.*, 26, 1781-1802,
482 <https://doi.org/10.1002/jcc.20289>, 2005.
- 483 Rissanen, M. P., Kurtén, T., Sipilä, M., Thornton, J. A., Kangasluoma, J., Sarnela, N., Junninen, H., Jørgensen, S.,
484 Schallhart, S., Kajos, M. K., Taipale, R., Springer, M., Mentel, T. F., Ruuskanen, T., Petäjä, T., Worsnop, D. R.,
485 Kjaergaard, H. G., and Ehn, M.: The Formation of Highly Oxidized Multifunctional Products in the Ozonolysis of
486 Cyclohexene, *J. Am. Chem. Soc.*, 136, 15596-15606, <https://doi.org/10.1021/ja507146s>, 2014.
- 487 Sakamoto, Y., Inomata, S., and Hirokawa, J.: Oligomerization Reaction of the Criegee Intermediate Leads to Secondary
488 Organic Aerosol Formation in Ethylene Ozonolysis, *J. Phys. Chem. A*, 117, 12912-12921,
489 <https://doi.org/10.1021/jp408672m>, 2013.
- 490 Shen, J., Elm, J., Xie, H.-B., Chen, J., Niu, J., and Vehkamäki, H.: Structural Effects of Amines in Enhancing
491 Methanesulfonic Acid-Driven New Particle Formation, *Environ. Sci. Technol.*, 54, 13498-13508,
492 <https://doi.org/10.1021/acs.est.0c05358>, 2020.
- 493 Stone, D., Blitz, M., Daubney, L., Howes, N. U. M., and Seakins, P.: Kinetics of CH₂OO reactions with SO₂, NO₂, NO,
494 H₂O and CH₃CHO as a function of pressure, *Phys. Chem. Chem. Phys.*, 16, 1139-1149,
495 <https://doi.org/10.1039/C3CP54391A>, 2014.
- 496 Tang, B., Bai, Q., Fang, Y.-G., Francisco, J. S., Zhu, C., and Fang, W.-H.: Mechanistic Insights into N₂O₅-Halide
497 Ions Chemistry at the Air-Water Interface, *J. Am. Chem. Soc.*, 146, 21742-21751,
498 <https://doi.org/10.1021/jacs.4c05850>, 2024.
- 499 Tröstl, J., Chuang, W. K., Gordon, H., Heinritzi, M., Yan, C., Molteni, U., Ahlm, L., Frege, C., Bianchi, F., Wagner, R.,
500 Simon, M., Lehtipalo, K., Williamson, C., Craven, J. S., Duplissy, J., Adamov, A., Almeida, J., Bernhammer, A.-K.,
501 Breitenlechner, M., Brilke, S., Dias, A., Ehrhart, S., Flagan, R. C., Franchin, A., Fuchs, C., Guida, R., Gysel, M.,
502 Hansel, A., Hoyle, C. R., Jokinen, T., Junninen, H., Kangasluoma, J., Keskinen, H., Kim, J., Krapf, M., Kürten, A.,
503 Laaksonen, A., Lawler, M., Leiminger, M., Mathot, S., Möhler, O., Nieminen, T., Onnela, A., Petäjä, T., Piel, F. M.,
504 Miettinen, P., Rissanen, M. P., Rondo, L., Sarnela, N., Schobesberger, S., Sengupta, K., Sipilä, M., Smith, J. N.,
505 Steiner, G., Tomè, A., Virtanen, A., Wagner, A. C., Weingartner, E., Wimmer, D., Winkler, P. M., Ye, P., Carslaw, K.
506 S., Curtius, J., Dommen, J., Kirkby, J., Kulmala, M., Riipinen, I., Worsnop, D. R., Donahue, N. M., and Baltensperger,
507 U.: The role of low-volatility organic compounds in initial particle growth in the atmosphere, *Nature*, 533, 527-531,
508 <https://doi.org/10.1038/nature18271>, 2016.
- 509 Tsona Tchinda, N., Du, L., Liu, L., and Zhang, X.: Pyruvic acid, an efficient catalyst in SO₃ hydrolysis and effective
510 clustering agent in sulfuric-acid-based new particle formation, *Atmos. Chem. Phys.*, 22, 1951-1963,
511 <https://doi.org/10.5194/acp-22-1951-2022>, 2022.
- 512 Wang, H., Wei, S., Yang, J., Yang, Y., Li, R., Wang, R., Zhu, C., Zhang, T., and Zhang, C.: A novel formation mechanism
513 of sulfamic acid and its enhancing effect on methanesulfonic acid-methylamine aerosol particle formation in



- 514 agriculture-developed and coastal industrial areas, *Atmos. Chem. Phys.*, 25, 2829-2844,
515 <https://doi.org/10.5194/acp-25-2829-2025>, 2025.
- 516 Wang, R., Wen, M., Chen, X., Mu, R., Zeng, Z., Chai, G., Lily, M., Wang, Z., and Zhang, T.: Atmospheric Chemistry
517 of CH₂OO: The Hydrolysis of CH₂OO in Small Clusters of Sulfuric Acid, *J. Phys. Chem. A*, 125, 2642-2652,
518 <https://doi.org/10.1021/acs.jpca.1c02006>, 2021a.
- 519 Wang, R., Wen, M., Liu, S., Lu, Y., Makroni, L., Muthiah, B., Zhang, T., Wang, Z., and Wang, Z.: The favorable routes
520 for the hydrolysis of CH₂OO with H₂O_n (*n* = 1-4) investigated by global minimum searching combined with quantum
521 chemical methods, *Phys. Chem. Chem. Phys.*, 23, 12749-12760, <https://doi.org/10.1039/D0CP00028K>, 2021b.
- 522 Wang, S., Zhao, Y., Chan, A. W. H., Yao, M., Chen, Z., and Abbatt, J. P. D.: Organic Peroxides in Aerosol: Key Reactive
523 Intermediates for Multiphase Processes in the Atmosphere, *Chem. Rev.*, 123, 1635-1679,
524 <https://doi.org/10.1021/acs.chemrev.2c00430>, 2023.
- 525 Wei, S., Wan, Q., Zhou, S., Nie, W., and Chen, S.: Spontaneous Generation of ⁻CH₂CN from Acetonitrile at the Air-Water
526 Interface, *J. Am. Chem. Soc.*, 146, 32777-32784, <http://doi.org/10.1021/jacs.4c13013>, 2024.
- 527 Wen, H., Huang, T., Wang, C.-Y., Peng, X.-Q., Jiang, S., Liu, Y.-R., and Huang, W.: A study on the microscopic mechanism
528 of methanesulfonic acid-promoted binary nucleation of sulfuric acid and water, *Atmos. Environ.*, 191, 214-226,
529 <https://doi.org/10.1016/j.atmosenv.2018.07.050>, 2018.
- 530 Wu, H., Fu, Y., Dong, W., Fu, B., and Zhang, D. H.: Full-dimensional neural network potential energy surface and
531 dynamics of the CH₂OO + H₂O reaction, *RSC Adv.*, 13, 13397-13404, <https://doi.org/10.1039/D3RA02069J>, 2023a.
- 532 Wu, H., Fu, Y., Fu, B., and Zhang, D. H.: Roaming Dynamics in Hydroxymethyl Hydroperoxide Decomposition Revealed
533 by the Full-Dimensional Potential Energy Surface of the CH₂OO + H₂O Reaction, *J. Phys. Chem. A*, 127, 9098-
534 9105, <https://doi.org/10.1021/acs.jpca.3c05818>, 2023b.
- 535 Wu, N., Ning, A., Liu, L., Zu, H., Liang, D., and Zhang, X.: Methanesulfonic acid and iodosic acid nucleation: a novel
536 mechanism for marine aerosols, *Phys. Chem. Chem. Phys.*, 25, 16745-16752, <https://doi.org/10.1039/d3cp01198d>,
537 2023c.
- 538 Xu, J., Finlayson-Pitts, B. J., and Gerber, R. B.: Nanoparticles grown from methanesulfonic acid and methylamine:
539 microscopic structures and formation mechanism, *Phys. Chem. Chem. Phys.*, 19, 31949-31957,
540 <https://doi.org/10.1039/d3cp01198d>, 2017a.
- 541 Xu, J., Finlayson-Pitts, B. J., and Gerber, R. B.: Proton Transfer in Mixed Clusters of Methanesulfonic Acid, Methylamine,
542 and Oxalic Acid: Implications for Atmospheric Particle Formation, *J. Phys. Chem. A*, 121, 2377-2385,
543 <https://doi.org/10.1021/acs.jpca.7b01223>, 2017b.
- 544 Xu, Q., Ma, F., Xia, D., Li, X., Chen, J., Xie, H.-B., and Francisco, J. S.: Two-Step Noncatalyzed Hydrolysis Mechanism
545 of Imines at the Air-Water Interface, *J. Am. Chem. Soc.*, 146, 28866-28873, <https://doi.org/10.1021/jacs.4c09080>,
546 2024.
- 547 Yan, J., Jung, J., Zhang, M., Xu, S., Lin, Q., Zhao, S., and Chen, L.: Significant Underestimation of Gaseous
548 Methanesulfonic Acid (MSA) over Southern Ocean, *Environ. Sci. Technol.*, 53, 13064-13070,
549 <https://doi.org/10.1021/acs.est.9b05362>, 2019.
- 550 Yi, M. J. R. o. E. S.: The Study on Pollution of Atmospheric Photochemical Oxidants in Beijing, *Res. Environ. Sci.* 13,
551 14-17., https://en.cnki.com.cn/Article_en/CJFDTOTAL-HJXX200001003.htm, 2000.
- 552 Zhang, J., and Dolg, M.: ABCluster: the artificial bee colony algorithm for cluster global optimization, *Phys. Chem. Chem.*
553 *Phys.*, 17, 24173-24181, <https://doi.org/10.1039/C5CP04060D>, 2015.
- 554 Zhang, R., Khalizov, A., Wang, L., Hu, M., and Xu, W.: Nucleation and Growth of Nanoparticles in the Atmosphere,
555 *Chem. Rev.*, 112, 1957-2011, <https://doi.org/10.1021/cr2001756>, 2012.



- 556 Zhang, R., Shen, J., Xie, H. B., Chen, J., and Elm, J.: The role of organic acids in new particle formation from
557 methanesulfonic acid and methylamine, *Atmos. Chem. Phys.*, 22, 2639-2650, [https://doi.org/10.5194/acp-22-](https://doi.org/10.5194/acp-22-2639-2022)
558 [2639-2022](https://doi.org/10.5194/acp-22-2639-2022), 2022.
- 559 Zhang, T., Lan, X., Wang, R., Roy, S., Qiao, Z., Lu, Y., and Wang, Z.: The catalytic effects of H₂CO₃, CH₃COOH, HCOOH
560 and H₂O on the addition reaction of CH₂OO + H₂O → CH₂(OH)OOH, *Mol. Phys.*, 116, 1783-1794,
561 <https://doi.org/10.1080/00268976.2018.1454612>, 2018.
- 562 Zhang, Y., ma, Y., Zeng, L., Shao, K., and Qi, B.: Study of atmospheric peroxides in Guangzhou city, *China Environ. Sci.*,
563 21, 221-225, https://en.cnki.com.cn/Article_en/CJFDTOTAL-ZGHJ200103008.htm, 2001.
- 564 Zhang, Z., Yin, H., Shang, Y., and Luo, S.-N.: Accurate rate constants for barrierless dissociation of ethanol: VRC-VTST
565 and SS-QRRK calculations with the cheaper DFT method, *Chem. Phys. Lett.*, 823, 140522,
566 <https://doi.org/10.1016/j.cplett.2023.140522>, 2023.
- 567 Zhang, Z. P., Wang, S. H., Shang, Y. L., Liu, J. H., and Luo, S. N.: Theoretical Study on Ethylamine Dissociation
568 Reactions Using VRC-VTST and SS-QRRK Methods, *J. Phys. Chem. A*, 128, 2191-2199,
569 <https://doi.org/10.1021/acs.jpca.3c08373>, 2024.
- 570 Zhao, H., Jiang, X., and Du, L.: Contribution of methane sulfonic acid to new particle formation in the atmosphere,
571 *Chemosphere*, 174, 689-699, <https://doi.org/10.1016/j.chemosphere.2017.02.040>, 2017.



MSA: methanesulfonic acid MA: methylamine HMHP: hydroxymethyl hydroperoxide

572

573

Graphic Abstract

574



575

Figure Captions

576 **Fig. 1** Potential energy surface for the hydrolysis of CH_2OO without (a) and with H_2O (b) and $\text{CH}_3\text{SO}_3\text{H}$ (c) at the
577 CCSD(T)-F12/cc-pVDZ-F12//M06-2X/6-311++G(2df,2pd) level

578 **Fig. 2** BOMD simulation trajectories and snapshots for $\text{CH}_3\text{SO}_3\text{H}$ -mediated CH_2OO hydration at the water
579 microdroplet interface

580 **Fig. 3** (a) Electrostatic potential (ESP)-mapped molecular van der Waals (vdW) surface of MA, HMHP, and MSA
581 calculated at M06-2X/6-311++G(2df, 2pd) + aug-cc-pVTZ level of theory. The orange and blue dots indicate the
582 positions of ESP maximums and minimums (in $\text{kcal}\cdot\text{mol}^{-1}$), with the corresponding values labeled in red and blue
583 numbers, respectively. (b) The reduced density gradient (RDG) color-filled maps and isosurface of $(\text{MSA})_1\cdot(\text{MA})_1$,
584 $(\text{MSA})_1\cdot(\text{MA})_1\cdot(\text{HMHP})_1$, and $(\text{MSA})_1\cdot(\text{MA})_1\cdot(\text{HMHP})_2$ clusters.

585 **Fig. 4** Gibbs free energies of formation for the growing clusters in MSA-MA-HMHP system as a function of growth
586 step at 258.15 K

587 **Fig. 5** Nucleation mechanism of the HMHP-MSA-MA system. (a) Cluster formation pathway at different
588 temperatures; (b) the branch ratio of outward flux under varying $[\text{MSA}]$ (1.0×10^4 - 1.0×10^8 $\text{molecules}\cdot\text{cm}^{-3}$); and
589 (c) enhancement of the cluster formation rate (J , $\text{cm}^{-3}\text{ s}^{-1}$).

590 **Fig. 6** The branch ratio of the MSA-MA-HMHP (blue pie) and MSA-MA (light blue pie) growth pathways based
591 on field data in different regions with a different $[\text{HMHP}]$. The data recorded in blue are from field observations,
592 and those in black are set to be a median in this study. $[\text{MA}] = 2.5 \times 10^8$ $\text{molecules}\cdot\text{cm}^{-3}$. The map is from ©Google
593 Maps (<https://www.google.com/maps>, last access: 15 July 2025).

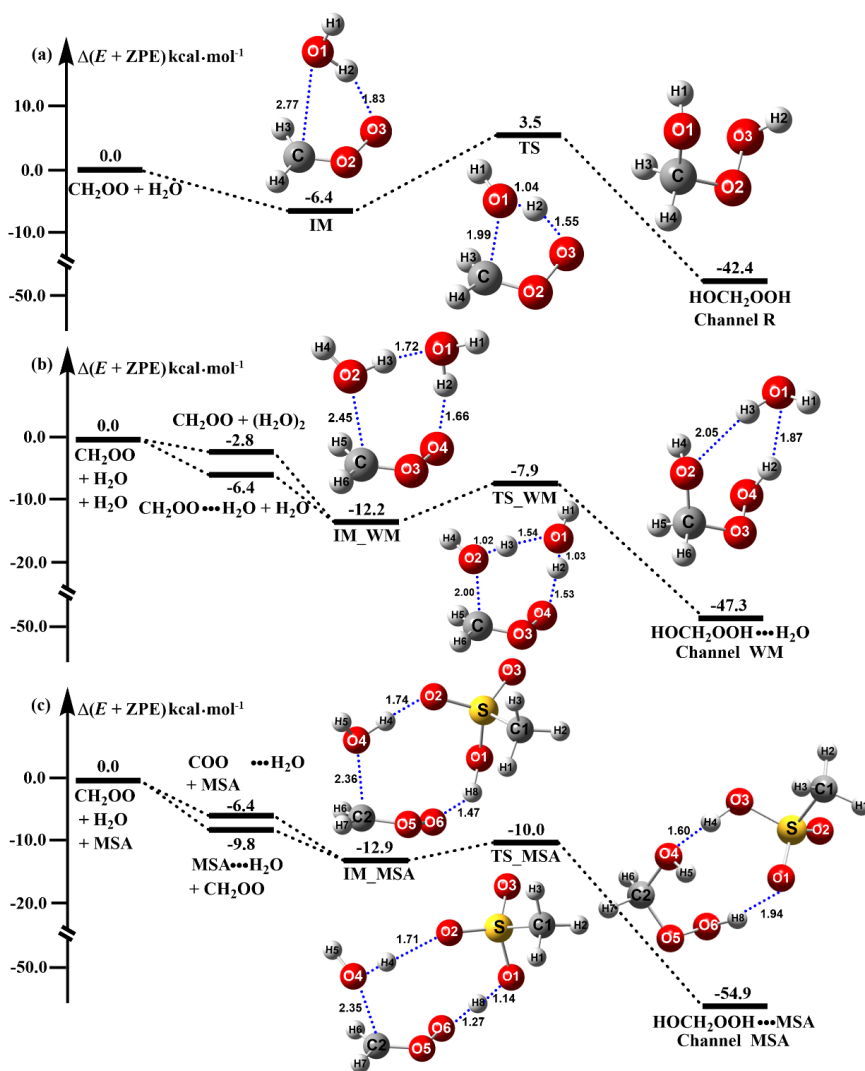


Fig. 1

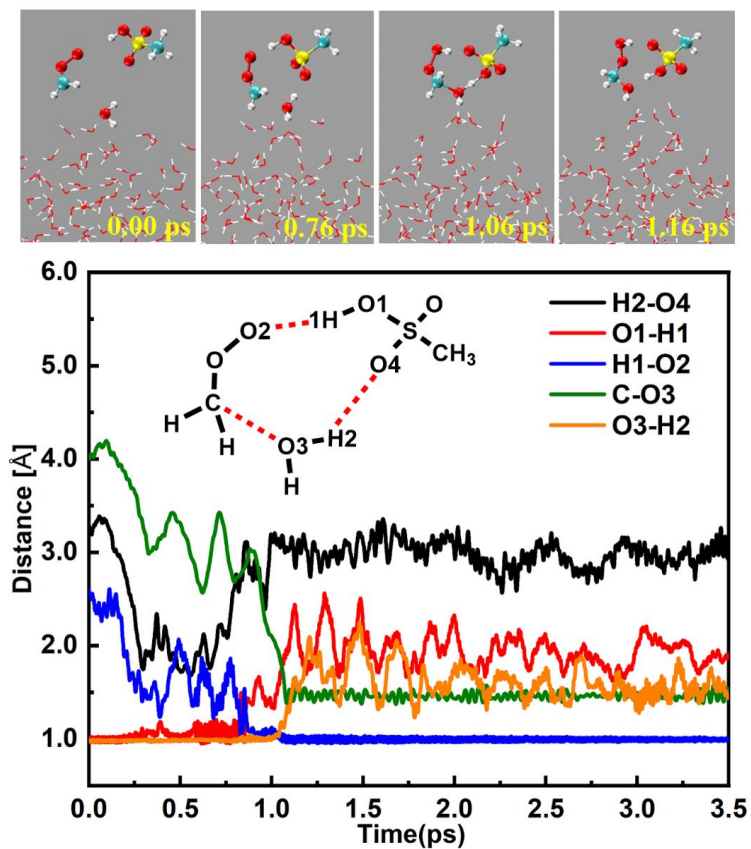


Fig. 2

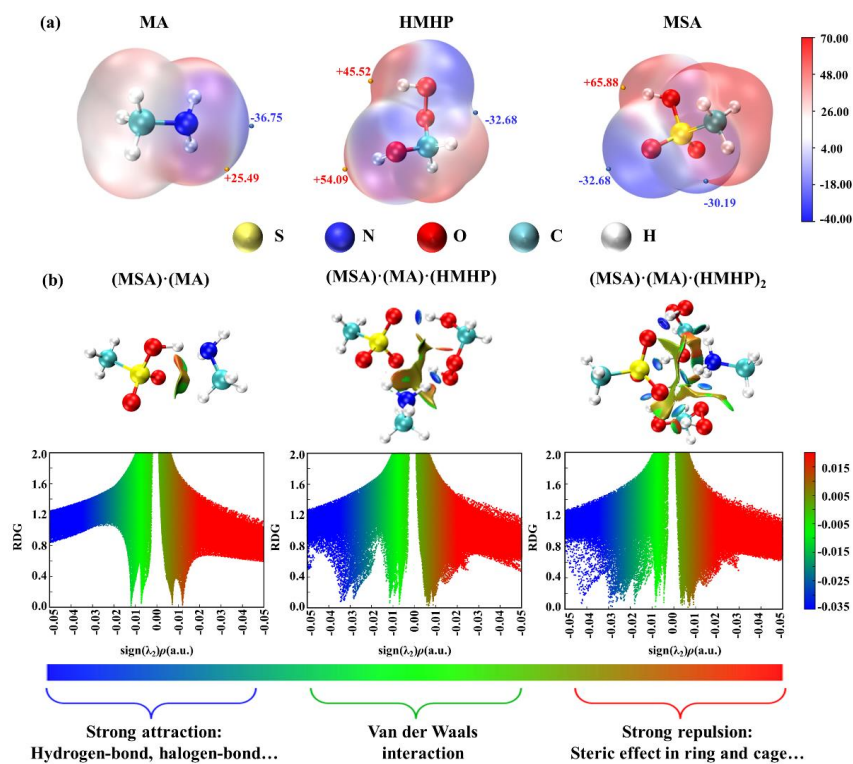


Fig. 3

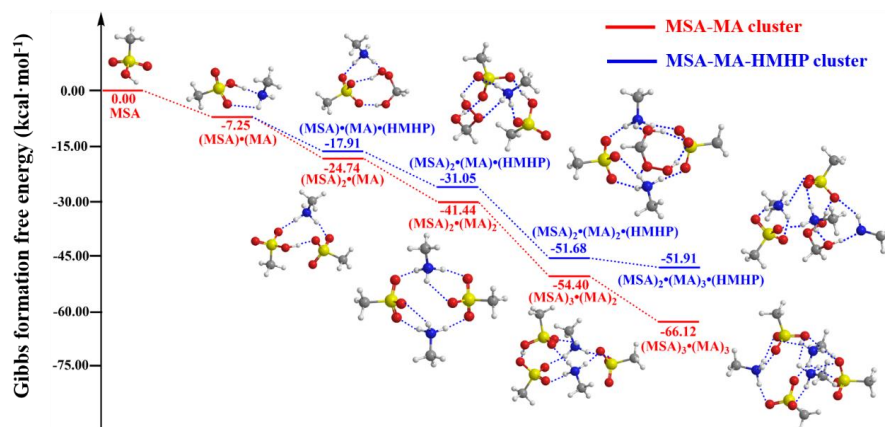


Fig. 4



(a) Cluster formation pathway ($[MSA] = 1.0 \times 10^6$; $[MA] = 2.5 \times 10^8$; $[HMHP] = 1.0 \times 10^{11}$ molecules·cm⁻³)

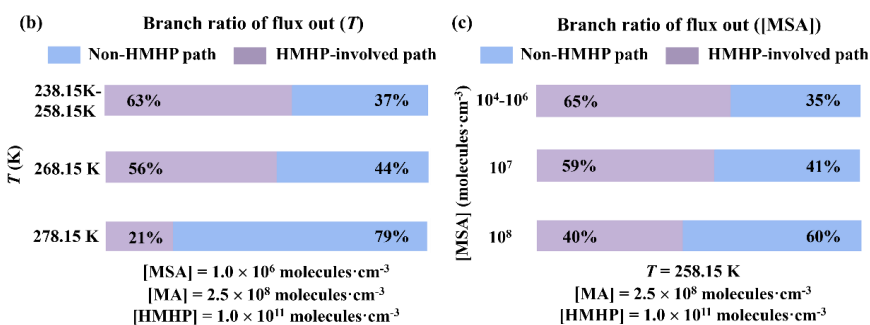
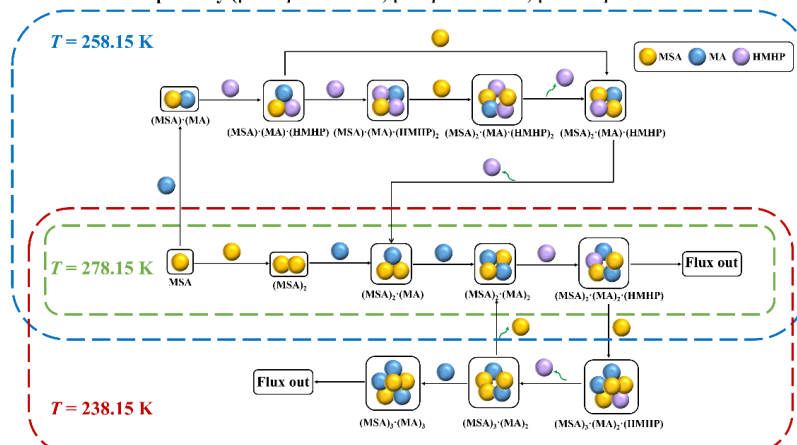


Fig. 5

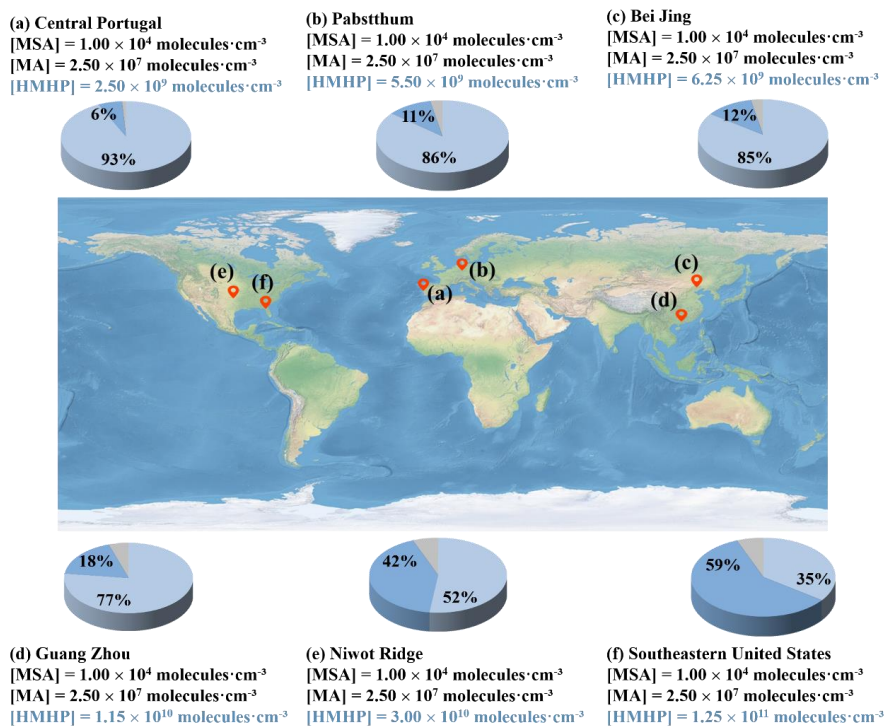


Fig.6



Table 1 The rate ratio (r_1) between the interfacial MSA-catalyzed CH₂OO hydrolysis reaction and the corresponding reaction in the gas phase as well as the rate ratio (r_2) between the MSA-catalyzed CH₂OO hydrolysis reaction at the air-water nanodroplet interface and the hydrolysis of CH₂OO facilitated by H₂O in the gas phase at 298.0 K.

Rate ratio	r_1	r_2
	1.01×10^2	13.4